

# Dynamics of Polyalkylfluorene Conjugated Polymers: Insights from Neutron Spectroscopy and Molecular Dynamics Simulations

Mohamed Zbiri<sup>\*,†</sup> and Anne A. Y. Guilbert<sup>\*,‡</sup>

E-mail: zbiri@ill.fr; a.guilbert09@imperial.ac.uk

## Abstract

Dynamics of the conjugated polymers poly(9,9-dioctylfluorene) (PF8) and poly(9,9-didodecylfluorene) (PF12), differing by the length of their side chains, is investigated in the amorphous phase using temperature-dependent time-of-flight (ToF) quasielastic neutron scattering (QENS) technique. The neutron spectroscopy measurements are synergistically underpinned by molecular dynamics (MD) simulations. The focus is put on probing the picosecond time scale where the structural dynamics would mostly be dominated by motions of the side chains. Within the instrumental accessible phase space, the neutron measurements highlighted temperature-induced dynamics reflected in the broadening of the QENS spectra upon heating. The MD simulations reproduced well the observations, hence the neutron measurements validate the MD force fields as well as the adopted amorphous model structures and numerical procedure. As the QENS spectra are mainly dominated by the signal from the different hydrogens on the backbones and side chains of PF8 and PF12, extensive analysis of the MD

---

\*To whom correspondence should be addressed

<sup>†</sup>Institut Laue-Langevin, 71 Avenue des Martyrs, Grenoble Cedex 9 38042, France

<sup>‡</sup>Department of Physics, Imperial College London, Prince Consort Road, London SW7 2AZ, United Kingdom

simulations allowed: (i) tagging these hydrogens, (ii) estimating their contributions to the self part of the van Hove functions and hence to the QENS spectra, and (iii) determining the activation energies of these motions. PF12 is found to exhibit broader QENS spectra than PF8, signature of a more pronounced motions of the didodecyl side chains as compared to dioctyl chains of PF8. This is in agreement with the outcome of our MD analysis: (i) confirming a lower glass transition temperature range of PF12 compared to PF8, (ii) showing PF12 having a lower solid-state density than PF8, and (iii) highlighting lower activation energies of all the motions of PF12 in comparison with PF8. This study helped gaining insights into the temperature-induced side chains dynamics of the PF8 and PF12 conjugated polymers that influence their stability and thus could practically impact the performance of the optoelectronic active layer.

## Introduction

Conjugated polymer materials have received considerable attention over the last decades because they can be integrated in flexible and stretchable light-weight optoelectronic and bioelectronic devices<sup>1-3</sup> such as organic led emitting diodes (OLEDs),<sup>4-7</sup> organic solar cells (OSCs),<sup>8-10</sup> organic field effect transistors (OFETs)<sup>11-14</sup> and more recently in organic electrochemical transistors (OECTs).<sup>15-17</sup> These devices could be in principle fabricated at low cost using roll-to-roll solution processing techniques. Initially, the development of conjugated polymers has focused on engineering the  $\pi$ -conjugated backbone as it gives rise to the optoelectronic properties of the material with the flexible side chains, mainly alkyl side chains, being primarily used as necessary solubilizing groups. Two very common molecular donor units found in conjugated polymer backbones and used as model systems are the thiophene ring and the fluorene unit. The fluorene unit comprises, in comparison with the simple thiophene ring, two aromatic rings that are planarized through the carbon bridging atom. Side chains have also been proven to have substantial impacts on the optoelectronic properties of conjugated polymers in the solid state. The solid-state morphology/microstructure

is significantly influenced by the choice of side chains as the solvent solubility impacts the processing and thus, the final packing. Also it has been shown that different side chains can modify the miscibility of the polymer with other components in blends. Length of side chains can modify the glass transition behaviour of the material. Often two glass transitions, one being assigned to the backbone and one to the side chains, are observed,<sup>18</sup> either due to microphase separation between backbone and side chains or decoupling of the segmental dynamics between the backbone and side chains even without microphase separation.<sup>19</sup> This can affect the stability of the active layer, especially blends where one component can diffuse through the side chains network, under operation i.e. thermal cycling. In other words, temperature-induced motions of both the side chain and backbone are important regarding the stability of the material. Generally, side chain dynamics - subject of the present work - take place on the picosecond time scale, while the backbone motions are slower and would occur within the nanosecond time window. Thus, structural dynamics of polymeric systems is both a time and temperature dependent behavior, whose characterization calls for appropriate temperature-dependent probe techniques.

Quasi-elastic neutron scattering (QENS) is a neutron spectroscopy technique, although offering an appropriate framework to probe microscopic time and length scales matching the structural dynamics of such materials, it is still underused in the field of organic semiconductors.<sup>20,21</sup> Pico-to-nanosecond exploration makes also QENS a method of choice to validate molecular dynamics (MD) models and simulations as well as to establish the usefulness of their associated force fields development.<sup>22-24</sup> The strength of QENS stems also from the neutron sensitivity to light elements. Neutrons interaction with hydrogen atoms dominate the incoherent neutron signal as hydrogen exhibits the strongest incoherent neutron scattering cross section. We demonstrated the usefulness of QENS, and other neutron spectroscopy techniques, as a tool to study the dynamics of organic semiconductors for different applications e.g. OSCs,<sup>21,22,25-28</sup> OFETs,<sup>29</sup> OECTs<sup>30</sup> and hydrogen production.<sup>31-33</sup> In particular, we used a combined approach of neutron spectroscopy and MD simulations to study dy-

namics of poly(3-hexylthiophene) (P3HT) and poly(3-octylthiophene) (P3OT) conjugated polymers,<sup>22</sup> followed by an extensive investigation of local and vibrational dynamics of P3HT under its two regio-regular (RR) and and regio-random (RRa) forms.<sup>27</sup>

Our previous work on the conjugated polymers P3HT and P3OT,<sup>22</sup> differing by the length of their alkyl side chains, highlighted a small difference in their dynamics around the glass transition temperature and around their respective melting point temperatures. The side chain length impacts on the poly(3-alkylthiophene) power conversion efficiencies when blended with phenyl-C61-butyric acid methyl ester(PCBM) was thus concluded to be linked to their different crystallization behavior. In this context, Zhan and coworkers went a step further by extending the dynamical study of the poly(3-aklythiophene) family to include poly(3-dodecylthiophene) (P3DDT), having a longer side chain than both P3HT and P3OT. They investigated primarily the effect of the side chain lengths on the backbone dynamics using neutron scattering techniques, NMR and MD simulations.<sup>34</sup>

Conjugated polymers are either semi-crystalline or amorphous materials. Their overall crystallinity is usually quite low, hence the amorphous phase plays an important role in their optoelectronic performances. On the computational side, structural modelling of the amorphous phase can be better controlled and optimized during the MD simulation process, targeting a resulting melt with a realistic time-resolved response to the temperature stimuli.<sup>22,26,27</sup>

In this work we extend the combined methodology of QENS and MD simulations to gain insights into the microstrutural dynamics of another class of conjugated polymers, namely poly(9,9-alkylfluorene). We select poly(9,9-dioctylfluorene) (PF8) and Poly(9,9-didodecylfluorene) (PF12) as model systems. Specifically, PF8 attracted interests due to its efficient deep-blue electroluminescence and high charge-carrier mobility for applications such as OLEDs and lasers. PF8 and PF12 differ by the length of their side chains (Figure 1(a)), therefore motivating us to probe their microstructural dynamics in their amorphous phase, with a focus to explore whether the side chain size difference would be reflected in their dynamics.

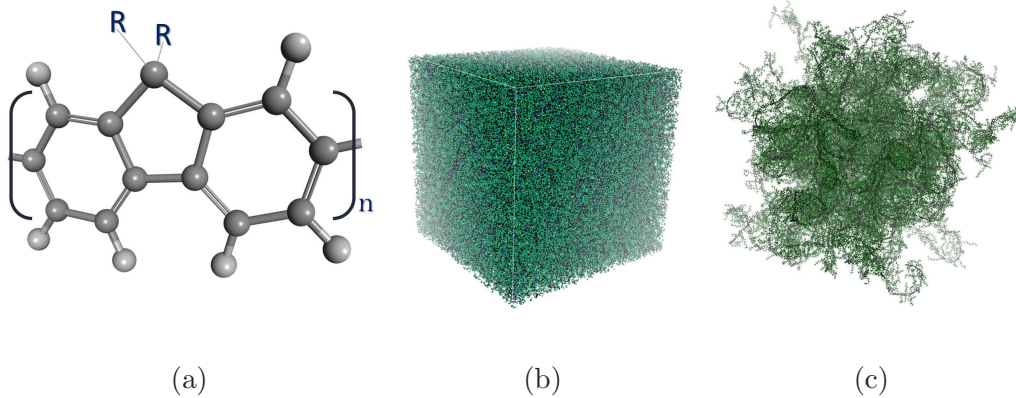


Figure 1: (a) Illustration of the chemical structure of the conjugated polymers poly(9,9-dioctylfluorene), PF8, and poly(9,9-didodecylfluorene), PF12. PF8 and PF12 differ by the length of their alkyl side chains i.e  $R=C_8H_{17}$  for PF8 and  $R=C_{12}H_{25}$  for PF12. (b) and (c) Representation of the resulting amorphous melt of either PF8 or PF12 from MD simulations with and without the MD boundary box, respectively.

## Results and discussion

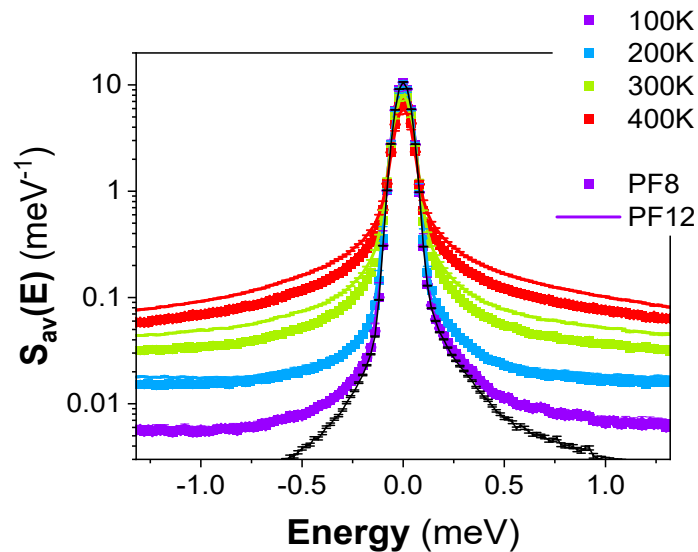


Figure 2: Temperature evolution of the measured Q-averaged quasielastic neutron scattering (QENS) spectra of PF8 (scatter points) and PF12 (solid line). The instrumental resolution (black line) is taken at base temperature for the same sample geometry.

The Q-averaged temperature-dependent QENS spectra of PF8 and PF12 are presented in Figure 2. A strong temperature-dependence is observed in terms of a decrease of the intensity of the elastic peak as temperature increases and a broadening of the QENS component. In other words, upon heating, dynamics are activated within the energy/time resolution of the instrument. If at both 100 K and 200 K, the Q-average QENS spectra of PF8 and PF12 are indiscernible, on the other hand, at 300 K and 400 K, PF12 exhibits a broader QENS component than PF8 with the associated reduction in the elastic contribution. Considering the instrumental picosecond time window coverage, we are likely to capture motions essentially linked to degrees of freedom of the side chains. Thus, above 300 K, the larger broadening of PF12 points towards faster motions of PF12 side chains in comparison with PF8. This could be due to various reasons including (i) motions involving hydrogens situated further away from the backbones and thus, experiencing a different environment, (ii) nano-phase segregation of backbones and side chains leading to the appearance of two glass transitions for longer side chains, and (iii) difference in microstructure e.g. packing, ordering, and crystallinity.

Numerical simulations have been proven, in addition to their predictive power, to play a key role in analyzing and interpreting experiments on conjugated polymers.<sup>35-37</sup> In this context, in order to gain insights into our observations, alike in our previous works,<sup>22,26,27</sup> we further carry out MD simulations to underpin the experimental data. The simulation boxes are equilibrated from the melt of both PF8 and PF12 (see experimental section), and are therefore largely amorphous (Figure 1(b,c)).

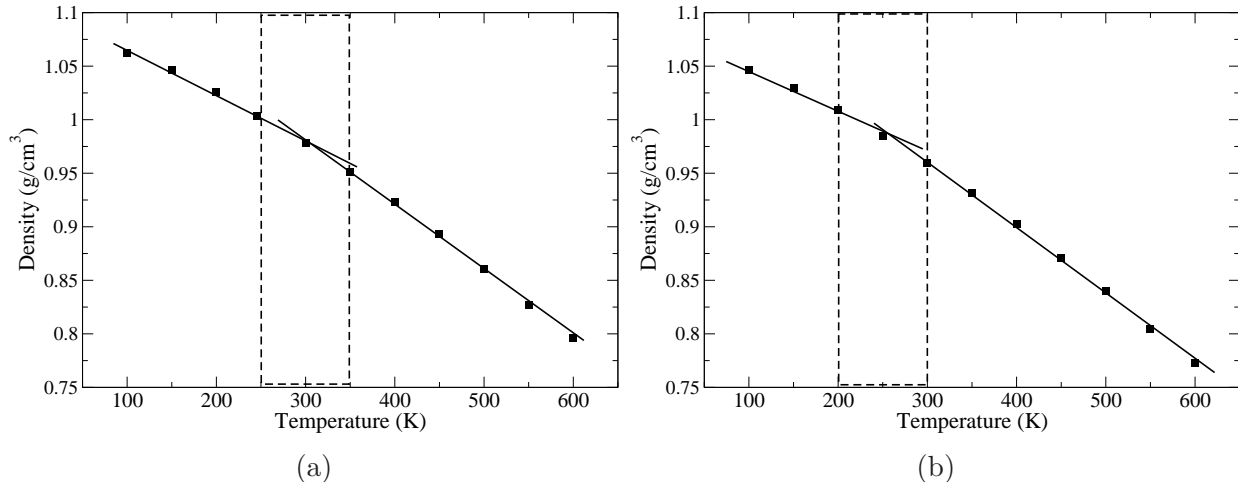


Figure 3: Temperature-dependent densities of (a) PF8 and (b) PF12 from MD simulations. The dashed rectangular area emphasizes the temperature range where a change in slope is observed.

The reliability of the produced trajectories from the MD simulations can be checked by extracting the density at each temperature (Figure 3). The density increases with reducing temperature. A change in the slope is observed between 250 and 350 K for PF8 (Figure 3(a)), and between 200 and 300 K for PF12 (Figure 3(b)). This suggests that the glass transition lies between 250 and 350 K for PF8, which is in good agreement with differential scanning calorimetry measurements,<sup>38</sup> and between 200 and 300 K for PF12. The glass transition is expected to decrease as the side chain mass fraction is increasing.<sup>19</sup> The density at 300 K is about 0.98 g/cm<sup>3</sup> for PF8 and 0.96 g/cm<sup>3</sup> for PF12.

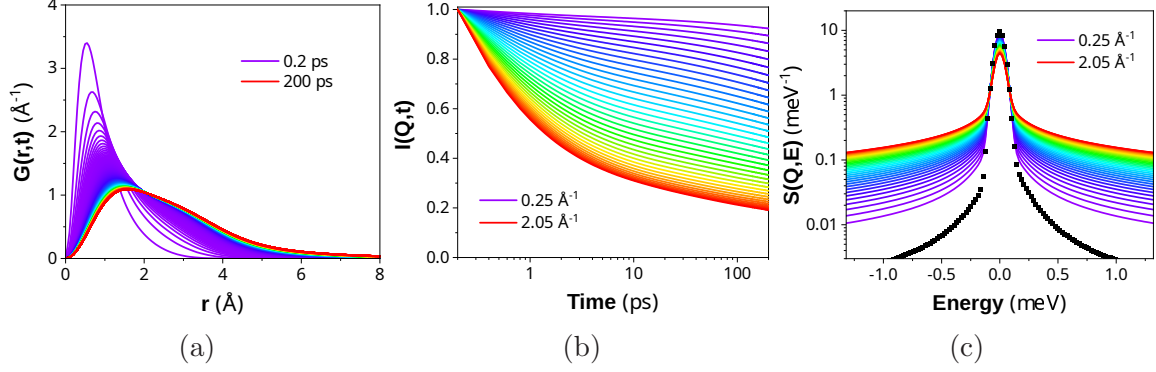


Figure 4: From MD calculations to simulated QENS spectra, exemplified by the case of PF8 at 400 K: (a) first, the MD trajectories are exploited to extract the time-resolved self-part of the Van Hove function,  $G(\mathbf{r},t)$ , at targeted temperatures. Here,  $G(\mathbf{r},t)$  was calculated for the time range 0.2 - 200 ps. (b) Subsequently, a space ( $\mathbf{r}$ ) to momentum transfer ( $\mathbf{Q}$ ) Fourier transform is applied to  $G(\mathbf{r},t)$  to derive the intermediate scattering function  $I(\mathbf{Q},t)$ . (c) Finally, the  $\mathbf{Q}$ -dependent QENS spectra,  $S(\mathbf{Q},E)$ , are obtained by convolution of the time ( $t$ ) to energy ( $E$ ) Fourier transform of  $I(\mathbf{Q},t)$  with an approximate instrumental resolution (black line). Both the simulated  $\mathbf{Q}$ -range (0.25 - 2.05  $\text{\AA}^{-1}$ ) and approximate resolution line match the respective experimental counterparts.

To relate the simulations to the QENS spectra, we extract the self-part of the Van Hove function  $G(\mathbf{r}, t)$  (Figure 4(a)).  $G(\mathbf{r}, t)$  is the probability density of finding a particle  $i$  at a position  $\mathbf{r}$ , at a time  $t$ , knowing that this particle was in the same position at the reference time  $t=0$ .  $G(\mathbf{r}, t)$  is expressed as:

$$G(\mathbf{r}, t) = \frac{1}{N} \left\langle \sum_{i=0}^N \delta(\mathbf{r} - \mathbf{r}_i(t) + \mathbf{r}_i(0)) \right\rangle \quad (1)$$

The Fourier transform in space of  $G(\mathbf{r}, t)$  gives the intermediate scattering function  $I(\mathbf{Q}, t)$  (Figure 4(b)):

$$I(\mathbf{Q}, t) = \int d\mathbf{r} G(\mathbf{r}, t) e^{-i\mathbf{Q}\cdot\mathbf{r}} \quad (2)$$

Finally, the dynamical structure factor  $S(\mathbf{Q}, E)$  can be calculated by Fourier transform of  $I(\mathbf{Q}, t)$  and a subsequent convolution with the instrumental resolution  $R(\mathbf{Q}, E)$  (Figure 4(c)):

$$S(\mathbf{Q}, E) = R(\mathbf{Q}, E) \otimes \int dt I(\mathbf{Q}, t) e^{-i\hbar\omega t} \quad (3)$$



Additional windowing is applied prior to the Fourier transform in space to take into consideration the accessible experimental Q-range.  $S(\mathbf{Q}, E)$  can be further averaged over the Q-range for comparison with Q-averaged experimental  $S_{av}(E)$ .

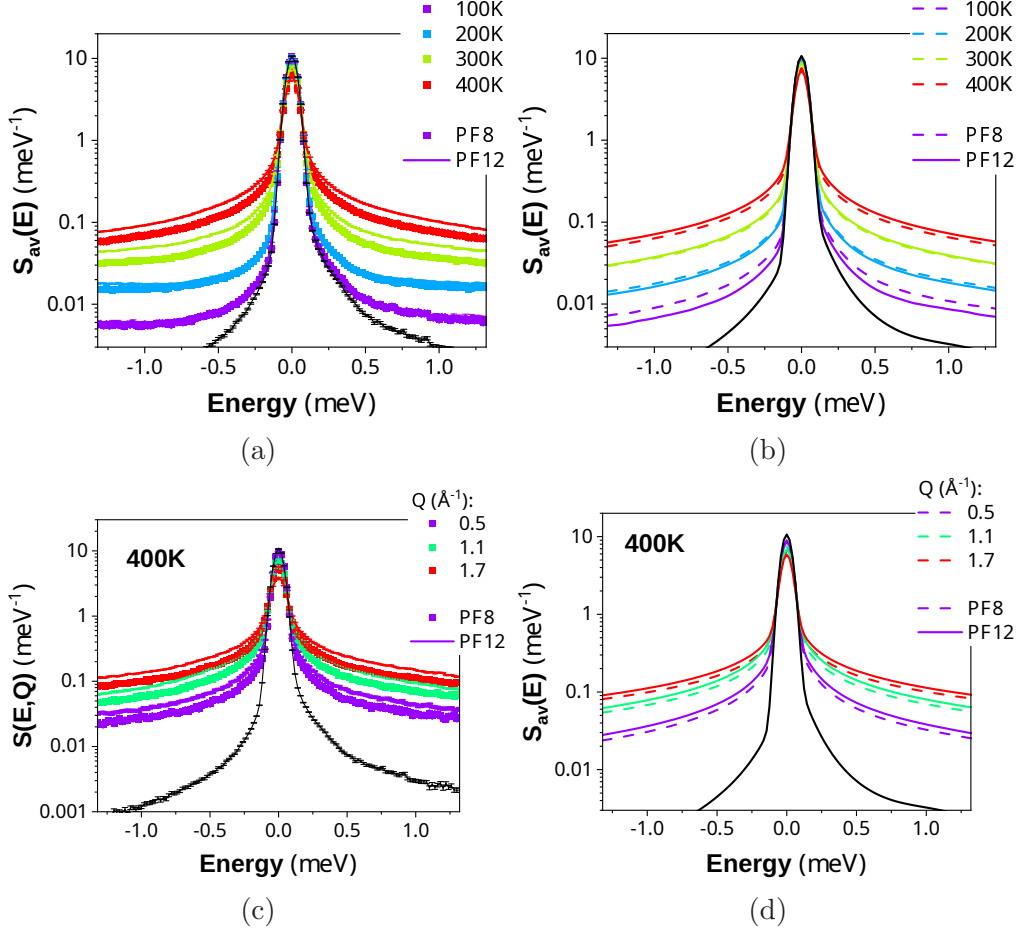


Figure 5: Comparison of the experimental and simulated QENS spectra of PF8 (points) and PF12 (line): (a) and (b) show the temperature evolution of the measured and simulated Q-averaged QENS spectra, respectively, while (c) and (d) display the Q dependence of the measured and simulated QENS spectra for specific Q points at 400K. The instrumental resolution (black line) is measured at base temperature for the same sample geometry in (a) and (c), while it is approximated in (b) and (d) matching the measured one.

Figure 5 shows a direct comparison between the measured and MD-based simulated QENS spectra. This concerns both the temperature-evolution of the spectra (Figure 5(a) vs Figure 5(b)) and their Q-dependence at 400 K for specific Q points (Figure 5(c) vs Figure 5(d)). On the one hand, the Q-averaged spectra offers a global view on the temperature-

induced activation of dynamics entering the experimental time window via the temperature evolution of the QENS spectra; on the other hand the Q-dependence of the QENS spectra at a given dynamics-activated temperature provides insights into the geometrical nature of underlying motions. First, the trend of the temperature evolution of the QENS spectra for both PF8 and PF12 is well reproduced by the MD simulations in terms of the spectral broadening and peaks intensities (Figure 5 (a) and (b)). The simulated Q-averaged QENS spectra at 300 K and 400 K are broader for PF12 than PF8, reproducing the observations, although the difference at 300 K is less pronounced as from the measurements. The simulated Q-averaged QENS spectra of PF8 and PF12 are close to each other at 200 K as in the experiment. However, the simulated QENS spectra of PF8 shows a slighter broadening than PF12 at 100 K, not observed experimentally. Second, the trend of experimental Q dependence of the QENS spectra at 400 K for selected Q points covering the experimentally accessible Q-range ( $\sim 0.2 - 2.1 \text{ \AA}^{-1}$ ) is also well reproduced numerically (Figure 5 (c) and (d)). Indeed, PF12 is found to exhibit broader QENS spectra than PF8 for all the Q points, and, as expected, QENS spectra of both PF8 and PF12 become broader as Q increases. This shows that the longer are the alkyl side chains, the more flexible they are, and the wider is the explored space by the associated increased translational motions of the protons along the chains, in a consistent way with other reports.<sup>22,34</sup>

The simulated QENS spectra are globally broader than the experimental ones, especially at lower temperatures. This could be due to: (i) the density of the simulation box being lower than the experimental density, (ii) limitations of the force fields parametrization, especially at the lowest temperatures, as common force fields are parameterized against macroscopic values measured at room temperature, and (iii) additional phases present in the measured samples and not accounted for numerically. However, the fact that the experimentally observed trend of the temperature evolution and Q-dependence of the measured QENS spectra is preserved and reliably well reproduced numerically allows us to further analyse the outcome of the MD simulations to gain insights into the observed dynamics of PF8 and PF12.

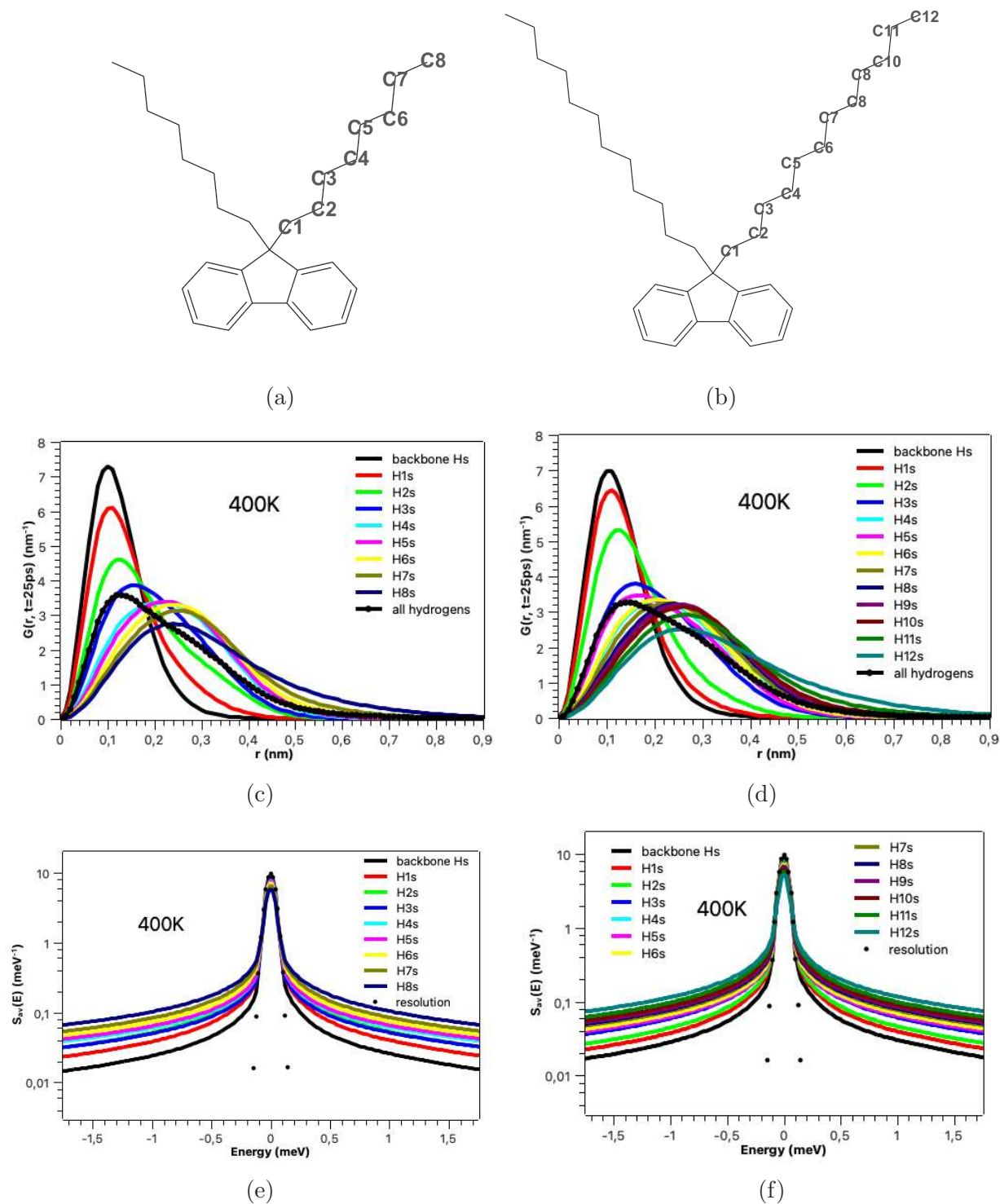


Figure 6: (a) and (b) Labeling of the side chain carbons of PF8 and PF12, respectively, to help assign the corresponding hydrogen-resolved contributions shown in (c), (d), (e) and (f). (c) and (d) Self-part of the van Hove function  $G(r, t = 25ps)$  of the different hydrogens (hydrogens on the backbones and hydrogens along the side chains) of PF8 and PF12, respectively, extracted from MD simulations at 400 K and a time step of 25 ps approximating the finite spread of the experimental time window. All hydrogens refers to the weighted average of all the hydrogen contributions to  $G(r, t = 25ps)$ . (e) and (f) Q-averaged QENS spectra obtained as per depicted in Figure 4<sup>11</sup> for the different hydrogens of PF8 and PF12, respectively.

The high incoherent neutron scattering cross section of hydrogens leads to a much stronger incoherent neutron scattering signal than that stemming from the neutron interaction with carbon atoms, which are mainly coherent scatterers. Hence, QENS is dominated by the signal of protons. As the present study deals with fully protonated samples, poly(9,9-alkylfluorene) has 6 hydrogens on the backbones, and 34 hydrogens and 50 hydrogens on the side chains per fluorene unit of PF8 and PF12, respectively. Interestingly, MD allows us to atomistically tag the different hydrogens to which carbons are bound to along the side chains and on the backbones of PF8 (Figure 6(a)) and PF12 (Figure 6(b)). This tagging can help gaining further insights into possible differences in motions as reflected in the hydrogen-resolved self part of the van Hove function  $G(r,t)$ , involving equivalent hydrogens in either PF8 (Figure 6(c)) or PF12 (Figure 6(d)), as well as in the associated QENS spectra shown in (Figure 6(e)) and (Figure 6(f)), respectively. This contrasted behavior of the different hydrogen contributions inferred from MD simulations underpins the measurements as it could be at the origin of the observed differences in the measured QENS spectra.

As specific motions enter the instrumental time window and others are too slow to be experimentally resolved, the corresponding hydrogen contributions at the origin of the activation of dynamics of PF8 and PF12 can be quantitatively compared (Figure 7). At 100 K (Figure 7(a)), the hydrogens on the backbones have motions too slow to be captured by the instrumental time window, as it can be seen by the overlap of the partial distribution of QENS spectra for both PF8 and PF12 with the instrumental resolution. At 100 K, the partial contribution to the Q-average spectra from the hydrogens in the middle of the side chains, namely H4 and H6 for PF8 and PF12, respectively, and of the methyl groups, namely H8 and H12 for PF8 and PF12, respectively, at the end of the side chains of PF8 and PF12 are similar. Although PF12 has more carbons along the side chains than PF8, a similar broadening is observed for equivalent hydrogens. As the temperature increases to 300 K (Figure 7(b)), the hydrogen-resolved QENS spectra of the backbones and the closer part of the side chains exhibit similar broadening for PF8 and PF12. However, the hydrogens

further away from the backbones start triggering slightly broader QENS spectra for PF12 as exemplified by the methyl groups contribution. At 400 K (Figure 7(c)), the hydrogens on the backbones contribute to the Q-average QENS spectra and the partial contributions of the equivalent hydrogens seems consistently broader for PF12 than PF8. This is also reflected in the small differences in Van Hove function for equivalent hydrogens of PF8 (Figures 6(c)) and PF12 (Figures 6(d)) at 400 K. At this temperature, it appears clearly that most of the hydrogens exhibit motions entering the instrumental window, within the experimental Q-range and energy range. The closer hydrogens are to the backbone, the narrower is their spatial distribution and subsequently the narrower is their QENS component. At 100 K (see Supporting Information), the hydrogens are more localised with most of hydrogens staying within an Angstrom from their initial positions, this is mainly vibrational motions. The Van Hove function for the hydrogens on the methyl group at 100 K shows the existence of two populations with the second population moving to up to 3 Angstroms.

We further analyze the outcome of the MD simulations by first fitting the simulated Q-averaged QENS spectra for the different hydrogens using the following model (see Supporting Information):

$$S_{av}(E) = R(E) \otimes (\delta(E = 0) + \mathcal{L}(E)) + b \quad (4)$$

where  $R(E)$  is the resolution,  $b$  is a constant background and  $\mathcal{L}(E)$  is a Lorentzian function defined as:

$$\mathcal{L}(E) = \frac{A}{\pi} * \frac{HWHM}{(E - E0)^2 + HWHM^2} \quad (5)$$

where  $A$  is the area of the Lorentzian  $\mathcal{L}$  centered around the energy  $E0$ , which should be equal to zero in the present case, and  $HWHM$  is the half-width at half-maximum. We can extract from the  $\delta$  function,  $\mathcal{L}$  and  $b$  the percentage of motions of each type of protons that: (i) are not experimentally resolved (too slow), (ii) are within the experimental window, and (iii) are too fast to be captured by the instrument (including thermally-induced molecular vibrational modes),<sup>27</sup> respectively.

Then, we proceed with fitting the dihedral autocorrelation functions (DACF) extracted from the MD simulations for the dihedral angles corresponding to the intermonomer torsion, i.e. the backbone torsion between different repeat units, and all the motions along the side chains (see Supporting Information) using a stretched exponential improved Lipari-Szabo model:<sup>39</sup>

$$DACF(t) = S_D^2 + (1 - S_D^2) \exp\left(-\frac{t^{\beta=0.5}}{\tau}\right) \quad (6)$$

where  $t$  denotes the time,  $S_D^2$  is the dihedral order parameter,<sup>40</sup> and  $\tau$  refers to the relaxation time of the rotation around the bond associated with the dihedral angle. While the Lipari-Szabo model<sup>39</sup> performs well at high temperatures, it is of a limited quality at low temperatures justifying the use of a stretched exponential for the sake of improvement.<sup>22</sup> A value of 0.5 for the exponent  $\beta$  is a reasonable choice for polymeric systems.<sup>41</sup> We also established previously that this value improved the fit quality especially at temperatures where motions are being activated, probably due to heterogeneities.<sup>22,27</sup>  $S_D^2$  is calculated from the dihedral distribution  $p(\theta)$  using the following equation:<sup>40</sup>

$$S_D^2 = \left[ \int_0^{2\pi} d\theta \cos(\theta) p(\theta) \right]^2 + \left[ \int_0^{2\pi} d\theta \sin(\theta) p(\theta) \right]^2 \quad (7)$$

Hence, the sole fitting parameter for the DACF is the relaxation time  $\tau$ , which is extracted for the different studied temperatures (see Supporting Information). Further, we fit the temperature-dependence of the relaxation time  $\tau$  of a specific motion (see Supporting Information) using a simple Arrhenius law:

$$\tau = \tau_0 \exp\left(-\frac{Ea}{k_B T}\right) \quad (8)$$

where  $Ea$  is the activation energy of that motion and  $k_B$  the Boltzmann constant. The larger broadening of the QENS spectra of PF12 at higher temperatures is also consistent with its lower activation energies in comparison with PF8 for all the studied motions (Figure 7(d)).

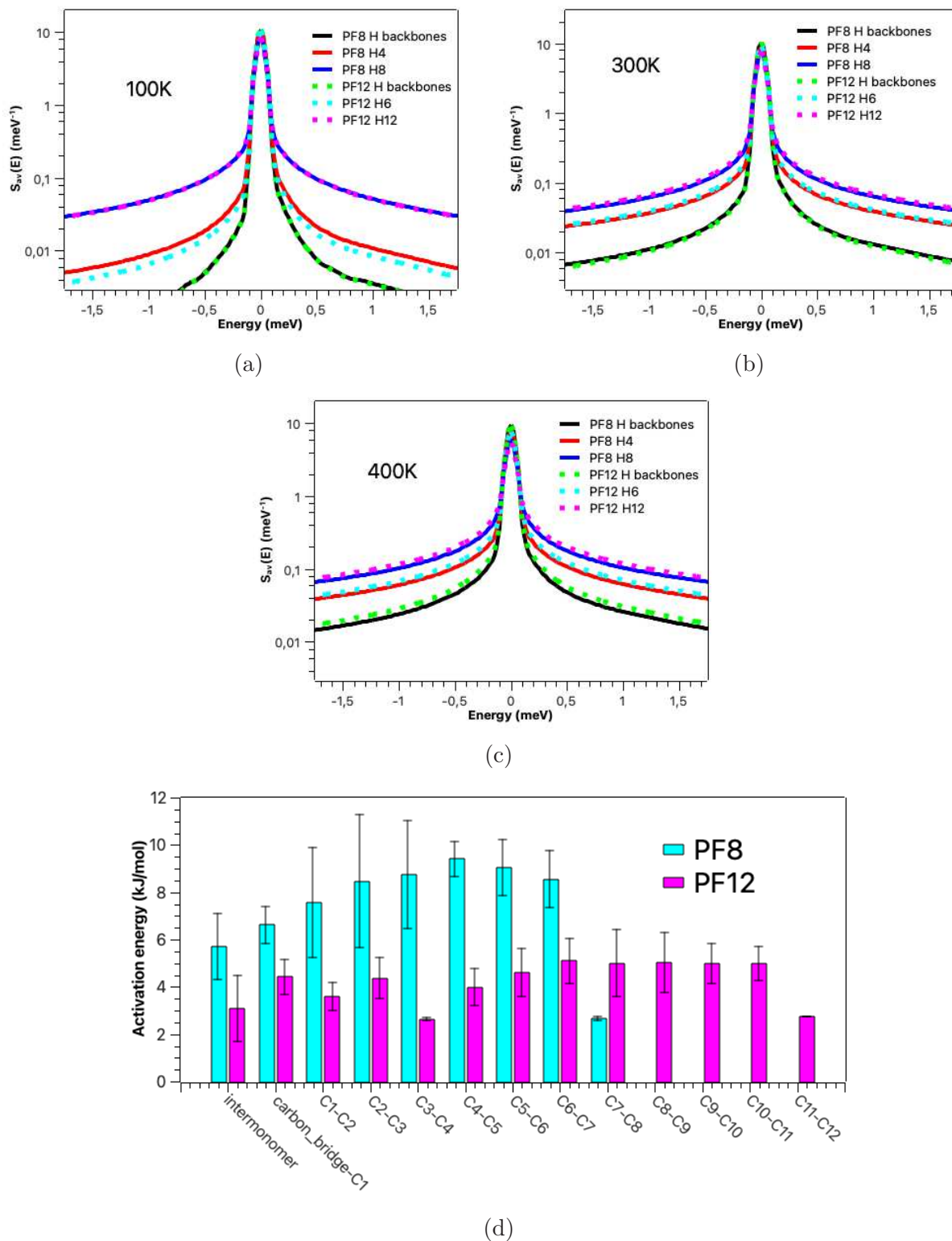


Figure 7: (a-c) Comparison of the simulated QENS spectra of PF8 (line) and PF12 (dots) for equivalent hydrogens at 100 , 300, and 400 K. (d) Activation energies for each motion for both PF8 and PF12.

# Conclusions

We used a combined approach of quasielastic neutron scattering (QENS) measurements and molecular dynamics (MD) simulations to gain insights into the microstructural dynamics of two polyalkylfluorene conjugated polymers differing by the length of their side chains, namely poly(9,9-dioctylfluorene) (PF8) and poly(9,9-didodecylfluorene) (PF12). The focus was put on exploring the picosecond time domain relevant to the dynamical degrees of freedom of the side chains in the amorphous phase. Neutrons being highly sensitive to hydrogen atoms, the QENS signal is mostly dominated by contributions from the different hydrogens of PF8 and PF12. MD simulations were used to underpin the neutron data for the sake of analysis and interpretation.

Within the instrumental time/energy ( $E$ ) window and the accessible momentum transfer ( $Q$ ) range, the neutron measurements highlighted both a temperature-induced and a  $Q$ -dependent broadening of the QENS spectra upon heating and as  $Q$  increases. The MD simulations reproduced well the observed behavior in terms of elastic peaks intensity decreasing concomitantly with the broadening of the QENS components. Hence, the used neutron technique validated the FF and MD simulation models and procedure, allowing to analyze reliably the observations.

The observed QENS broadening along with the decrease of the intensity of the elastic component for PF8 and PF12, also reproduced by MD simulations, is a signature of activated motions being captured and entering the instrumental time window. Further, PF12 is found to exhibit a broader  $Q$ -dependent QENS component than PF8, pointing towards a more pronounced dynamical behavior of the former. This shows that the longer side chains of PF12, being more flexible, explore a wider space through an increased motion of the protons from the backbone and along the chains. The extensive analysis we performed of the outcome of the MD simulations allowed also to quantitatively determine the temperature-dependent individual contributions of the different hydrogens, belonging to the backbones and side chains, to the observed motions of PF8 and PF12. We found that the more pronounced



dynamics of PF12 as compared to that of PF8 is also energetically favorable as due to the lower activation energies of all the motions of PF12 in comparison with PF8. This is also in agreement with a lower glass transition temperature<sup>19,38</sup> and a lower solid-state density of PF12 as compared to PF8.

In a consistent way with previous works focused on the effect of side chains size on the dynamical behavior of polyalkylthiophenes, this study helped gaining insights into side chains dynamics of polyalkylfluorenes, yet another important class of conjugated polymers. Dynamical behaviors of conjugated polymers are important to study as they relate to the stability of the active layer of the optoelectronic devices. The optoelectronic properties are impacted by the process of solubilizing these materials via different morphology developments during the drying process due to the side chains-solvent interaction leading to the subsequent final solid state microstructure. In this context, we started also exploring structural dynamics of polyalkylfluorenes with different solvents aiming at probing their crystalline  $\beta$  phase and the role of solvents in its emergence as compared to the presently reported solvent-free amorphous phase.

## Experimental and Computational Details

### Quasielastic Neutron Scattering

PF8 and PF12 were obtained from Sumitomo Chemical/Cambridge Display Technology (CDT) and Sigma-aldrich, respectively. PF8 and PF12 were used as received. The samples were in a first instance heated to 400 K in order to (i) remove any presence of PF8  $\beta$ -phase and any trace of solvents coming from synthesis that could promote the formation of  $\beta$ -phase upon cooling<sup>42</sup> as well as (ii) any water residuals that could invalidate the QENS results due to the high neutron cross-section of hydrogens.

The temperature-dependent picosecond QENS measurements were performed at the Institut Laue-Langevin (Grenoble, France) using the direct geometry cold neutron TOF spectrometer

IN5. An incident wavelength of 5.1 Å was used offering an energy resolution at the elastic line of  $\sim 0.08$  meV, and leading to a  $Q$ -range of  $\sim 0.2 - 2.1$  Å<sup>-1</sup>. Data were collected up to 400K and down to 2 K for instrumental resolution purpose at the same sample geometry. The measured samples were about 260 mg, and were sealed into thin annular aluminum containers with an optimized thickness of 0.2 mm relevant to minimizing effects like multiple scattering and absorption. Different temperature-dependent data sets were extracted, using standard ILL tools, either by performing a full  $Q$ -average in the  $(Q, E)$  space to get the scattering function  $S_{av}(E)$ , or by considering  $Q$ -slices to study the  $S(Q, E)$ .

## Molecular Dynamics Simulations

MD simulations were performed using Gromacs-5.1.3 package,<sup>43-49</sup> where a leapfrog algorithm was adopted. Periodic boundary conditions are applied in all directions. The Particle-mesh Ewald (PME) method is used for computing long-range electrostatic interactions. Depending on the ensemble NVT or NPT, we used a velocity-rescaling thermostat<sup>50</sup>(varying temperature, time constant 0.1 ps for equilibration and 0.5 ps for collection runs) and a Berendsen barostat (1 bar, compressibility  $4.5 \cdot 10^{-5} \text{bar}^{-1}$ , time constant 5 ps for equilibration and 2 ps for collection runs), respectively.

We developed our own polyfluorene force field that is available upon reasonable request. 100 chains of 20-mers of PF8/PF12 were built. This corresponds to a Mw of about 7.8 kDa for PF8 and 10.1 kDa for P12, respectively. Simulating longer chains while avoiding strong interaction between the images of the chains means increasing significantly the number of atoms and thus, the computational power needed for these calculations. However, given the accessible timescale by the experiments, we are likely measuring mainly the dynamics of the side chains, which justifies this choice.

The amorphous samples were prepared from the melt as follows:

- 100 chains were loosely and randomly packed using Packmol<sup>51</sup>

- the structures are relaxed through energy minimisation using the steepest descent algorithm. The convergence criterion was set such that the maximum force is smaller than  $10 \text{ kJ.mol}^{-1}.\text{nm}^{-1}$ .
- NVT run at  $T=2000\text{K}$  for 100 ps
- NPT run at  $T=600\text{K}$  and  $P=10000 \text{ bar}$  for 100 ps
- NPT run at  $T=600\text{K}$  and  $P=1\text{bar}$  for 5 ns
- NPT run at  $T=550\text{K}$  and  $P=1\text{bar}$  for 5 ns
- NPT run at  $T=500\text{K}$  and  $P=1\text{bar}$  for 5 ns
- ...
- NPT run at  $T=150\text{K}$  and  $P=1\text{bar}$  for 5 ns
- NPT run at  $T=100\text{K}$  and  $P=1\text{bar}$  for 5 ns

The size of the final boxes were checked to be larger than the length of an elongated 20mers of PF8/12 plus the cut-off radius used for the van der Waals forces (1.2 nm). For the temperature of interest, an extra collection run was produced in NPT for 5 ns, and only the last 4 ns were used for the analysis.

## Acknowledgement

X. Shi and J. Nelson are thanked for discussions regarding samples. This work was supported by EPSRC through grant EP/P005543/1.

## Supporting Information Available

Distribution of the dihedral angles from MD simulations at different temperatures. Temperature-dependent relaxation times of the different rotational motions of the side chains. Fits of the

hydrogen-resolved QENS spectra from MD simulations at different temperatures. Dihedral time-autocorrelation functions from MD simulations and associated fits at different temperatures. Hydrogen-resolved self-part of the van Hove functions from MD simulations at different temperatures.

## References

- (1) Chow, P. C. Y.; Someya, T. Organic Photodetectors for Next-Generation Wearable Electronics. *Advanced Materials* **2020**, *32*, 1902045, DOI: <https://doi.org/10.1002/adma.201902045>.
- (2) Kousseff, C. J.; Halaksa, R.; Parr, Z. S.; Nielsen, C. B. Mixed Ionic and Electronic Conduction in Small-Molecule Semiconductors. *Chemical Reviews* **2022**, *122*, 4397–4419, DOI: [10.1021/acs.chemrev.1c00314](https://doi.org/10.1021/acs.chemrev.1c00314), PMID: 34491034.
- (3) Chang, S.; Koo, J. H.; Yoo, J.; Kim, M. S.; Choi, M. K.; Kim, D.-H.; Song, Y. M. Flexible and Stretchable Light-Emitting Diodes and Photodetectors for Human-Centric Optoelectronics. *Chemical Reviews* **2024**, *124*, 768–859, DOI: [10.1021/acs.chemrev.3c00548](https://doi.org/10.1021/acs.chemrev.3c00548), PMID: 38241488.
- (4) Geffroy, B.; le Roy, P.; Prat, C. Organic light-emitting diode (OLED) technology: materials, devices and display technologies. *Polymer International* **2006**, *55*, 572–582, DOI: <https://doi.org/10.1002/pi.1974>.
- (5) Thejo Kalyani, N.; Dhoble, S. Organic light emitting diodes: Energy saving lighting technology—A review. *Renewable and Sustainable Energy Reviews* **2012**, *16*, 2696–2723, DOI: <https://doi.org/10.1016/j.rser.2012.02.021>.
- (6) Salehi, A.; Fu, X.; Shin, D.-H.; So, F. Recent Advances in OLED Optical Design. *Advanced Functional Materials* **2019**, *29*, 1808803, DOI: <https://doi.org/10.1002/adfm.201808803>.

- (7) Hong, G.; Gan, X.; Leonhardt, C.; Zhang, Z.; Seibert, J.; Busch, J. M.; Bräse, S. A Brief History of OLEDs—Emitter Development and Industry Milestones. *Advanced Materials* **2021**, *33*, 2005630, DOI: <https://doi.org/10.1002/adma.202005630>.
- (8) Holliday, S.; Ashraf, R. S.; Wadsworth, A.; Baran, D.; Yousaf, S. A.; Nielsen, C. B.; Tan, C.-H.; Dimitrov, S. D.; Shang, Z.; Gasparini, N.; Alamoudi, M.; Laquai, F.; Brabec, C. J.; Salleo, A.; Durrant, J. R.; McCulloch, I. High-efficiency and air-stable P3HT-based polymer solar cells with a new non-fullerene acceptor. *Nature Communications* **2016**, *7*, 11585, DOI: [10.1038/ncomms11585](https://doi.org/10.1038/ncomms11585).
- (9) Cui, Y.; Yao, H.; Zhang, J.; Xian, K.; Zhang, T.; Hong, L.; Wang, Y.; Xu, Y.; Ma, K.; An, C.; He, C.; Wei, Z.; Gao, F.; Hou, J. Single-Junction Organic Photovoltaic Cells with Approaching 18% Efficiency. *Advanced Materials* **2020**, *32*, 1908205, DOI: <https://doi.org/10.1002/adma.201908205>.
- (10) Zhang, G.; Lin, F. R.; Qi, F.; Heumüller, T.; Distler, A.; Egelhaaf, H.-J.; Li, N.; Chow, P. C. Y.; Brabec, C. J.; Jen, A. K.-Y.; Yip, H.-L. Renewed Prospects for Organic Photovoltaics. *Chemical Reviews* **2022**, *122*, 14180–14274, DOI: [10.1021/acs.chemrev.1c00955](https://doi.org/10.1021/acs.chemrev.1c00955), PMID: 35929847.
- (11) Oh, J. Y.; Rondeau-Gagné, S.; Chiu, Y.-C.; Chortos, A.; Lissel, F.; Wang, G.-J. N.; Schroeder, B. C.; Kurosawa, T.; Lopez, J.; Katsumata, T.; Xu, J.; Zhu, C.; Gu, X.; Bae, W.-G.; Kim, Y.; Jin, L.; Chung, J. W.; Tok, J. B.-H.; Bao, Z. Intrinsically stretchable and healable semiconducting polymer for organic transistors. *Nature* **2016**, *539*, 411–415, DOI: [10.1038/nature20102](https://doi.org/10.1038/nature20102).
- (12) Ocheje, M. U.; Comí, M.; Yang, R.; Chen, Z.; Liu, Y.; Yousefi, N.; Al-Hashimi, M.; Rondeau-Gagné, S. Molecular engineering of benzothiadiazole-based polymers: balancing charge transport and stretchability in organic field-effect transistors. *J. Mater. Chem. C* **2022**, *10*, 4236–4246, DOI: [10.1039/D1TC06103H](https://doi.org/10.1039/D1TC06103H).

- (13) Yang, Y.-T.; Wu, Y.-S.; He, W.; Tien, H.-C.; Yang, W.-C.; Michinobu, T.; Chen, W.-C.; Lee, W.-Y.; Chueh, C.-C. Tuning Ambipolarity of the Conjugated Polymer Channel Layers of Floating-Gate Free Transistors: From Volatile Memories to Artificial Synapses. *Advanced Science* **2022**, *9*, 2203025, DOI: <https://doi.org/10.1002/advs.202203025>.
- (14) Yu, X.; Chen, L.; Li, C.; Gao, C.; Xue, X.; Zhang, X.; Zhang, G.; Zhang, D. Intrinsically Stretchable Polymer Semiconductors with Good Ductility and High Charge Mobility through Reducing the Central Symmetry of the Conjugated Backbone Units. *Advanced Materials* **2023**, *35*, 2209896, DOI: <https://doi.org/10.1002/adma.202209896>.
- (15) Rivnay, J.; Inal, S.; Salleo, A.; Owens, R. M.; Berggren, M.; Malliaras, G. G. Organic electrochemical transistors. *Nature Reviews Materials* **2018**, *3*, 17086, DOI: [10.1038/natrevmats.2017.86](https://doi.org/10.1038/natrevmats.2017.86).
- (16) Borges-González, J.; Kousseff, C. J.; Nielsen, C. B. Organic semiconductors for biological sensing. *J. Mater. Chem. C* **2019**, *7*, 1111–1130, DOI: [10.1039/C8TC05900D](https://doi.org/10.1039/C8TC05900D).
- (17) Wu, X.; Li, Z.; Hu, J.; Wang, S.; Wang, Y.; Lin, P.; Zhou, H.; Zhao, W.-W. Metallointercalated-DNA Nanotubes as Functional Light Antenna for Organic Photoelectrochemical Transistor Biosensor with Minimum Background. *Analytical Chemistry* **2023**, *95*, 11800–11806, DOI: [10.1021/acs.analchem.3c02258](https://doi.org/10.1021/acs.analchem.3c02258), PMID: 37506318.
- (18) Qian, Z.; Cao, Z.; Galuska, L.; Zhang, S.; Xu, J.; Gu, X. Glass Transition Phenomenon for Conjugated Polymers. *Macromolecular Chemistry and Physics* **2019**, *220*, 1900062, DOI: <https://doi.org/10.1002/macp.201900062>.
- (19) Xie, R.; Weisen, A. R.; Lee, Y.; Aplan, M. A.; Fenton, A. M.; Masucci, A. E.; Kempe, F.; Sommer, M.; Pester, C. W.; Colby, R. H.; Gomez, E. D. Glass transition temperature from the chemical structure of conjugated polymers. *Nature Communications* **2020**, *11*, 893, DOI: [10.1038/s41467-020-14656-8](https://doi.org/10.1038/s41467-020-14656-8).

- (20) Cavaye, H. Neutron Spectroscopy: An Under-Utilised Tool for Organic Electronics Research? *Angewandte Chemie International Edition* **2019**, *58*, 9338–9346, DOI: <https://doi.org/10.1002/anie.201812950>.
- (21) Zbiri, M.; Gilhooly-Finn, P. A.; Fouquet, P.; Nielsen, C. B.; Guilbert, A. A. Y. Structural Dynamics of Polymer:Non-Fullerene Organic Solar Cell Blends: A Neutron Spectroscopy Perspective. *Chemistry of Materials* **2022**, *34*, 7937–7946, DOI: [10.1021/acs.chemmater.2c01705](https://doi.org/10.1021/acs.chemmater.2c01705).
- (22) Guilbert, A. A. Y.; Urbina, A.; Abad, J.; Díaz-Paniagua, C.; Batallán, F.; Seydel, T.; Zbiri, M.; García-Sakai, V.; Nelson, J. Temperature-Dependent Dynamics of Polyalkylthiophene Conjugated Polymers: A Combined Neutron Scattering and Simulation Study. *Chemistry of Materials* **2015**, *27*, 7652–7661, DOI: [10.1021/acs.chemmater.5b03001](https://doi.org/10.1021/acs.chemmater.5b03001).
- (23) Wolf, C. M.; Kanekal, K. H.; Yimer, Y. Y.; Tyagi, M.; Omar-Diallo, S.; Pakhnyuk, V.; Luscombe, C. K.; Pfaendtner, J.; Pozzo, L. D. Assessment of molecular dynamics simulations for amorphous poly(3-hexylthiophene) using neutron and X-ray scattering experiments. *Soft Matter* **2019**, *15*, 5067–5083, DOI: [10.1039/C9SM00807A](https://doi.org/10.1039/C9SM00807A).
- (24) Wolf, C. M.; Guio, L.; Scheiwiller, S.; Pakhnyuk, V.; Luscombe, C.; Pozzo, L. D. Strategies for the Development of Conjugated Polymer Molecular Dynamics Force Fields Validated with Neutron and X-ray Scattering. *ACS Polymers Au* **2021**, *1*, 134–152, DOI: [10.1021/acspolymersau.1c00027](https://doi.org/10.1021/acspolymersau.1c00027).
- (25) Guilbert, A.; Zbiri, M.; Jenart, M.; Nielsen, C.; Nelson, J. New Insights into the Molecular Dynamics of P3HT:PCBM Bulk Heterojunction: A Time-of-Flight Quasi-Elastic Neutron Scattering Study. *Journal of Physical Chemistry Letters* **2016**, *7*, DOI: [10.1021/acs.jpcllett.6b00537](https://doi.org/10.1021/acs.jpcllett.6b00537).
- (26) Guilbert, A.; Zbiri, M.; Dunbar, A.; Nelson, J. Quantitative Analysis of the Molecu-

- lar Dynamics of P3HT:PCBM Bulk Heterojunction. *Journal of Physical Chemistry B* **2017**, *121*, DOI: 10.1021/acs.jpcc.7b08312.
- (27) Guilbert, A. A.; Zbiri, M.; Finn, P. A.; Jenart, M.; Fouquet, P.; Cristiglio, V.; Frick, B.; Nelson, J.; Nielsen, C. B. Mapping Microstructural Dynamics up to the Nanosecond of the Conjugated Polymer P3HT in the Solid State. *Chemistry of Materials* **2019**, *31*, 9635–9651, DOI: 10.1021/acs.chemmater.9b02904.
- (28) Zbiri, M.; Finn, P. A.; Nielsen, C. B.; Guilbert, A. A. Y. Quantitative insights into the phase behaviour and miscibility of organic photovoltaic active layers from the perspective of neutron spectroscopy. *J. Mater. Chem. C* **2021**, *9*, 11873–11881, DOI: 10.1039/D1TC01813B.
- (29) Stoeckel, M.-A.; Olivier, Y.; Gobbi, M.; Dudenko, D.; Lemaure, V.; Zbiri, M.; Guilbert, A. A. Y.; D’Avino, G.; Liscio, F.; Migliori, A.; Ortolani, L.; Demitri, N.; Jin, X.; Jeong, Y.-G.; Liscio, A.; Nardi, M.-V.; Pasquali, L.; Razzari, L.; Beljonne, D.; Samorn, P.; Orgiu, E. Analysis of External and Internal Disorder to Understand Band-Like Transport in n-Type Organic Semiconductors. *Advanced Materials* **2021**, *33*, 2007870, DOI: <https://doi.org/10.1002/adma.202007870>.
- (30) Guilbert, A. A. Y.; Parr, Z. S.; Kreouzis, T.; Woods, D. J.; Sprick, R. S.; Abrahams, I.; Nielsen, C. B.; Zbiri, M. Effect of substituting non-polar chains with polar chains on the structural dynamics of small organic molecule and polymer semiconductors. *Phys. Chem. Chem. Phys.* **2021**, *23*, 7462–7471, DOI: 10.1039/D1CP00670C.
- (31) Sprick, R. S.; Bai, Y.; Guilbert, A. A. Y.; Zbiri, M.; Aitchison, C. M.; Wilbraham, L.; Yan, Y.; Woods, D. J.; Zwijnenburg, M. A.; Cooper, A. I. Photocatalytic Hydrogen Evolution from Water Using Fluorene and Dibenzothiophene Sulfone-Conjugated Microporous and Linear Polymers. *Chemistry of Materials* **2019**, *31*, 305–313, DOI: 10.1021/acs.chemmater.8b02833.



- (32) Guilbert, A. A. Y.; Bai, Y.; Aitchison, C. M.; Sprick, R. S.; Zbiri, M. Impact of Chemical Structure on the Dynamics of Mass Transfer of Water in Conjugated Microporous Polymers: A Neutron Spectroscopy Study. *ACS Applied Polymer Materials* **2021**, *3*, 765–776, DOI: 10.1021/acsapm.0c01070, PMID: 33615231.
- (33) Zbiri, M.; Aitchison, C. M.; Sprick, R. S.; Cooper, A. I.; Guilbert, A. A. Y. Probing Dynamics of Water Mass Transfer in Organic Porous Photocatalyst Water-Splitting Materials by Neutron Spectroscopy. *Chemistry of Materials* **2021**, *33*, 1363–1372, DOI: 10.1021/acs.chemmater.0c04425, PMID: 33840892.
- (34) Zhan, P.; Zhang, W.; Jacobs, I. E.; Nisson, D. M.; Xie, R.; Weissen, A. R.; Colby, R. H.; Moulé, A. J.; Milner, S. T.; Maranas, J. K.; Gomez, E. D. Side chain length affects backbone dynamics in poly(3-alkylthiophene)s. *Journal of Polymer Science Part B: Polymer Physics* **2018**, *56*, 1193–1202, DOI: <https://doi.org/10.1002/polb.24637>.
- (35) Bhat, V.; Callaway, C. P.; Risko, C. Computational Approaches for Organic Semiconductors: From Chemical and Physical Understanding to Predicting New Materials. *Chemical Reviews* **2023**, *123*, 7498–7547, DOI: 10.1021/acs.chemrev.2c00704, PMID: 37141497.
- (36) Yang, Q.; Vriza, A.; Castro Rubio, C. A.; Chan, H.; Wu, Y.; Xu, J. Artificial Intelligence for Conjugated Polymers. *Chemistry of Materials* **2024**, *0*, null, DOI: 10.1021/acs.chemmater.3c02358.
- (37) Alesadi, A.; Cao, Z.; Li, Z.; Zhang, S.; Zhao, H.; Gu, X.; Xia, W. Machine learning prediction of glass transition temperature of conjugated polymers from chemical structure. *Cell Reports Physical Science* **2022**, *3*, 100911, DOI: <https://doi.org/10.1016/j.xcrp.2022.100911>.
- (38) Shi, X.; Nádaždy, V.; Perevedentsev, A.; Frost, J. M.; Wang, X.; von Hauff, E.; MacKenzie, R. C. I.; Nelson, J. Relating Chain Conformation to the Density of States

- and Charge Transport in Conjugated Polymers: The Role of the  $\beta$ -phase in Poly(9,9-dioctylfluorene). *Phys. Rev. X* **2019**, *9*, 021038, DOI: 10.1103/PhysRevX.9.021038.
- (39) Lipari, G.; Szabo, A. Model-free approach to the interpretation of nuclear magnetic resonance relaxation in macromolecules. 1. Theory and range of validity. *Journal of the American Chemical Society* **1982**, *104*, 4546–4559, DOI: 10.1021/ja00381a009.
- (40) van der Spoel, D.; Berendsen, H. Molecular dynamics simulations of Leu-enkephalin in water and DMSO. *Biophysical Journal* **1997**, *72*, 2032–2041, DOI: [https://doi.org/10.1016/S0006-3495\(97\)78847-7](https://doi.org/10.1016/S0006-3495(97)78847-7).
- (41) Richter, D.; Monkenbusch, M.; Arbe, A.; Colmenero, J. *Neutron Spin Echo in Polymer Systems*; Springer Berlin Heidelberg: Berlin, Heidelberg, 2005; pp 67–78, DOI: 10.1007/b106578.
- (42) Perevedentsev, A.; Stavrinou, P. N.; Bradley, D. D. C.; Smith, P. Solution-crystallization and related phenomena in 9,9-dialkyl-fluorene polymers. I. Crystalline polymer-solvent compound formation for poly(9,9-dioctylfluorene). *Journal of Polymer Science Part B: Polymer Physics* **2015**, *53*, 1481–1491, DOI: <https://doi.org/10.1002/polb.23798>.
- (43) Berendsen, H.; van der Spoel, D.; van Drunen, R. GROMACS: A message-passing parallel molecular dynamics implementation. *Computer Physics Communications* **1995**, *91*, 43–56, DOI: 10.1016/0010-4655(95)00042-E.
- (44) Lindahl, E.; Hess, B.; van der Spoel, D. GROMACS 3.0: a package for molecular simulation and trajectory analysis. *Journal of Molecular Modeling* **2001**, *7*, 306–317, DOI: 10.1007/s008940100045.
- (45) Van Der Spoel, D.; Lindahl, E.; Hess, B.; Groenhof, G.; Mark, A. E.; Berendsen, H. J. C. GROMACS: Fast, flexible, and free. *Journal of Computational Chemistry* **2005**, *26*, 1701–1718, DOI: 10.1002/jcc.20291.

- (46) Hess, B.; Kutzner, C.; van der Spoel, D.; Lindahl, E. GROMACS 4: Algorithms for Highly Efficient, Load-Balanced, and Scalable Molecular Simulation. **2008**, *4*, 435–447, DOI: 10.1021/CT700301Q.
- (47) Pronk, S.; Páll, S.; Schulz, R.; Larsson, P.; Bjelkmar, P.; Apostolov, R.; Shirts, M. R.; Smith, J. C.; Kasson, P. M.; van der Spoel, D.; Hess, B.; Lindahl, E. GROMACS 4.5: a high-throughput and highly parallel open source molecular simulation toolkit. *Bioinformatics* **2013**, *29*, 845–854, DOI: 10.1093/bioinformatics/btt055.
- (48) Páll, S.; Abraham, M. J.; Kutzner, C.; Hess, B.; Lindahl, E. *Tackling Exascale Software Challenges in Molecular Dynamics Simulations with GROMACS*; Springer, Cham, 2015; pp 3–27, DOI: 10.1007/978-3-319-15976-8\_1.
- (49) Abraham, M. J.; Murtola, T.; Schulz, R.; Páll, S.; Smith, J. C.; Hess, B.; Lindahl, E. GROMACS: High performance molecular simulations through multi-level parallelism from laptops to supercomputers. *SoftwareX* **2015**, *1-2*, 19–25, DOI: 10.1016/J.SOFTX.2015.06.001.
- (50) Bussi, G.; Donadio, D.; Parrinello, M. Canonical sampling through velocity rescaling. *Journal of Chemical Physics* **2007**, *126*, 014101, DOI: 10.1063/1.2408420.
- (51) Martínez, L.; Andrade, R.; Birgin, E. G.; Martínez, J. M. PACKMOL: A package for building initial configurations for molecular dynamics simulations. *Journal of Computational Chemistry* **2009**, *30*, 2157–2164, DOI: 10.1002/jcc.21224.